

Article

On the Wake Properties of Segmented Trailing Edge Extensions

Sidaard Gunasekaran * and Daniel Curry

Department of Mechanical and Aerospace Engineering, University of Dayton, Dayton, OH 45469, USA; curryd1@udayton.edu

* Correspondence: gunasekarans1@udayton.edu; Tel.: +1-937-229-5345

Received: 14 July 2018; Accepted: 15 August 2018; Published: 21 August 2018



Abstract: Changes in the amount and the distribution of mean and turbulent quantities in the free shear layer wake of a 2D National Advisory Committee for Aeronautics (NACA) 0012 airfoil and an AR 4 NACA 0012 wing with passive segmented rigid trailing edge (TE) extensions were investigated at the University of Dayton Low Speed Wind Tunnel (UD-LSWT). The TE extensions were intentionally placed at zero degrees with respect to the chord line to study the effects of segmented extensions without changing the effective angle of attack. Force based experiments were used to determine the total lift coefficient variation of the wing with seven segmented trailing edge extensions distributed across the span. The segmented trailing edge extensions had a negligible effect on the lift coefficient, but showed a measurable decrement in the sectional and total drag coefficient. Investigation of turbulent quantities (obtained through Particle Image Velocimetry (PIV)) such as Reynolds stress, streamwise and transverse root-mean square (RMS) in the wake, reveal a significant decrease in magnitude when compared to the baseline. The decrease in the magnitude of turbulent parameters was supported by the changes in coherent structures obtained through two-point correlations. Apart from the reduction in drag, the lower turbulent wake generated by the extensions has implications in reducing structural vibrations and acoustic tones.

Keywords: trailing edge extensions; drag reduction; coherent structures

1. Introduction

The ideology of application of trailing edge extensions on streamlined bodies to affect wing performance dates to WWII where National Advisory Committee for Aeronautics (NACA) investigated the use of trailing edge (TE) extensions on propeller blades to change the camber and effective angle of attack of propeller sections [1]. Based on the extension geometry, orientation and the airfoil, the design coefficient of lift (CL) can be matched with the operating conditions of the propeller sections to obtain an optimum pressure distribution. Theodorsen and Stickle [1] derived theoretical expressions for the changes in effective angle of attack of the wing as a function of extension length and angle using thin airfoil theory, but validation of theoretical work with experimental work was not done until later. In 1989, Ito [2] performed experimental investigations to study the effect of trailing edge extensions on Göttingen 797 and Wortmann FX 63-137 airfoils used on earlier short-take off and landing (STOL) aircraft, at Reynolds numbers between 300,000 and 1,000,000. The extensions, when placed along the camber-line, significantly increased the CL max and Lift-to-Drag (L/D) ratio for Gö797, but didn't have any effect on the Wortmann airfoil due to its high camber and a complicated curved lower surface. This result indicated that the effectiveness of the TE extensions depend significantly on the airfoil profile.

This sensitivity on the effectiveness of TE extensions on the airfoil profile is due to angle of the free shear layer wake and characteristic turbulence. Most airfoils experience vortex shedding at the

trailing edge, resulting in a loss of total pressure, and hence drag increases. Similar to a cylinder, the vortex shedding behind a wing is a function of the Reynolds number, as shown in experiments done by Yarusevych et al. [3]. They determined that the roll-up of vortices in the separated shear layer play a key role in the flow transition to turbulence. The relationship between the flow separation and vortex shedding in an airfoil can be clearly seen in Figure 1 taken from Yarusevych et al. [3] where the smoke released downstream of the wing is seen upstream on top of the wing.

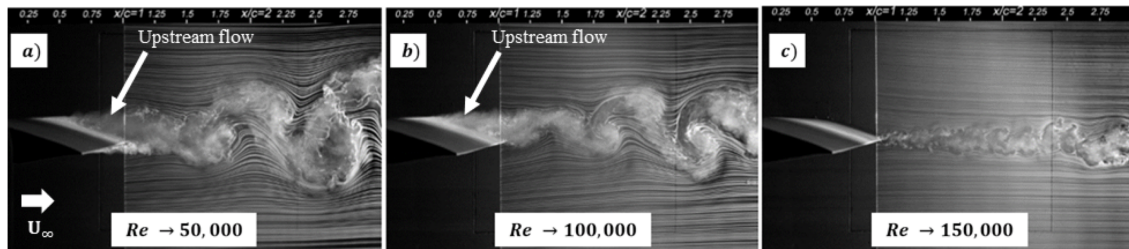


Figure 1. Shedding of vortices from the trailing edge of NACA 0025 airfoil at different Reynolds numbers (a) 50,000 (b) 100,000 (c) 150,000 (adapted from Yarusevych [3]).

Figure 1 shows prominent turbulent wake vortex shedding due to the separated upper surface shear layer. Huang and Lin [4] and Huang and Lee [5] performed experiments on the NACA 0012 airfoil and reported that vortex shedding is only observed at lower Reynolds numbers where boundary layer separation occurs without reattachment. Yarusevych et al. [3] amended this result and proved that vortex shedding occurs even after the boundary layer attaches to the surface at a higher Reynolds number, as shown in Figure 1c, and that vortex shedding varies linearly with the Reynolds number.

The vortex shedding is also found to be a function of trailing edge geometry. Guan et al. [6] experimented with multiple beveled trailing edge geometries and showed that even subtle changes in geometry can result in substantial changes in wake signature. The vortex shedding was found to be greater at the sharp trailing edge when compared to the rounded trailing edges, but even with a smooth trailing edge, the turbulent coherent structures were found to convect without distinguishing separation points into the wake, which complements the result from Yarusevych et al. [3].

The effectiveness of the TE extensions depends on the length and angle of the TE extension, the airfoil section, the effective angle of attack of the wing, chord based Reynolds number and trailing edge geometry. All of these parameters affect the vortex shedding behind the wing, which influences the parasitic drag experienced by the wing. The parasitic drag contribution on airplanes during cruise is in the order of 50% of the total drag [7]. The streamwise pressure gradient created by the periodic shedding of vortices initiates on-body flow separation, resulting in higher drag, undesirable structural vibrations and higher acoustic levels.

The current study is aimed at investigating the sensitivity of the segmented TE extensions on the amount and distribution of vorticity and the turbulent parameters in the free shear layer wake. Some techniques used to mitigate vortex shedding are shown below.

1.1. Vortex Mitigation Techniques

Most of the parasitic drag reduction methods on a wing are targeted at keeping the boundary layer attached and delaying the transition. A slew of active and passive flow control techniques involving laminar flow control, wall cooling, hybrid laminar flow control, active wave suppression, use of riblets, vortex generators, large eddy breakup devices, surface geometry effects such as streamwise and transverse curvatures and microgrooves, synthetic boundary layers, etc., were used to prevent boundary layer transition and separation. When compared to the number of methods available to mitigate vortex shedding from bluff bodies such as cylinders, trucks, cars, etc., the number of methods available to mitigate vortex shedding from streamlined bodies is minimal.

One of the popular methods to mitigate the influence of vortex shedding from a wing is the use of Gurney flaps or divergent trailing edges. A Gurney flap is an extension of the trailing edge in the direction perpendicular to the chord. The use of Gurney flaps generates a favorable streamwise pressure gradient at high angle of attack, and is known to shift the location of the separation from the leading edge to the quarter chord location while at the same time increasing lift on the main airfoil profile (Stanewsky [8]). A finite pressure differential is carried to the trailing edge and is sustained by a vortex shedding induced base pressure on the downstream face of the flap. Numerous computational and experimental works have been done to study the effect of length and angle of Gurney flaps on vortex shedding. (Neuhart and Pendergraft [9], Jang and Ross [10], Storms and Jang [11], Traub [12]). However, these flaps are usually more effective at higher angles of attack, where the flow separates and actually generates higher drag, as expected in areas where flow is not separated.

The disadvantage of higher drag using Gurney flaps at lower angles of attack can be overcome by having a static extended trailing edge (SETE) or flexible extended trailing edge (FETE).

Lui et al. [13] attached a thin flat plate at the trailing edge of a NACA 0012 airfoil made of aluminum and Mylar, determined the changes in the airfoil efficiency as a function of angle of attack, and compared it with the measurement made from the Gurney flap (Figure 2). SETE showed a larger lift increase at a smaller drag penalty, better than a Gurney flap, since the SETE was in between the wake of the main airfoil. SETE shows improvements in lift characteristics across the range of angles of attack when compared to Gurney flaps, where the lift improvement is seen only at higher angles of attack. Lui et al. [13] also determined the aeroelastic deformation for aluminum (less than 1%) and Mylar (13%) and postulated that MEMS microphones can be embedded in the SETE which will change and react to their surroundings. A similar approach is used in this research, but instead of using a SETE, a segmented TE extensions was used to conserve weight and reduce drag forces on the wing. Segmented TE extensions can also act as control surfaces, as was implemented by Lee and Kroo [14], where they placed microflaps or Miniature Trailing Edge Effectors (MiTEs) on the trailing edge of the high aspect ratio wings (Figure 3) to suppress flutter through dynamic deflection. With this type of controller, they were able to increase the flutter speed by 22%.

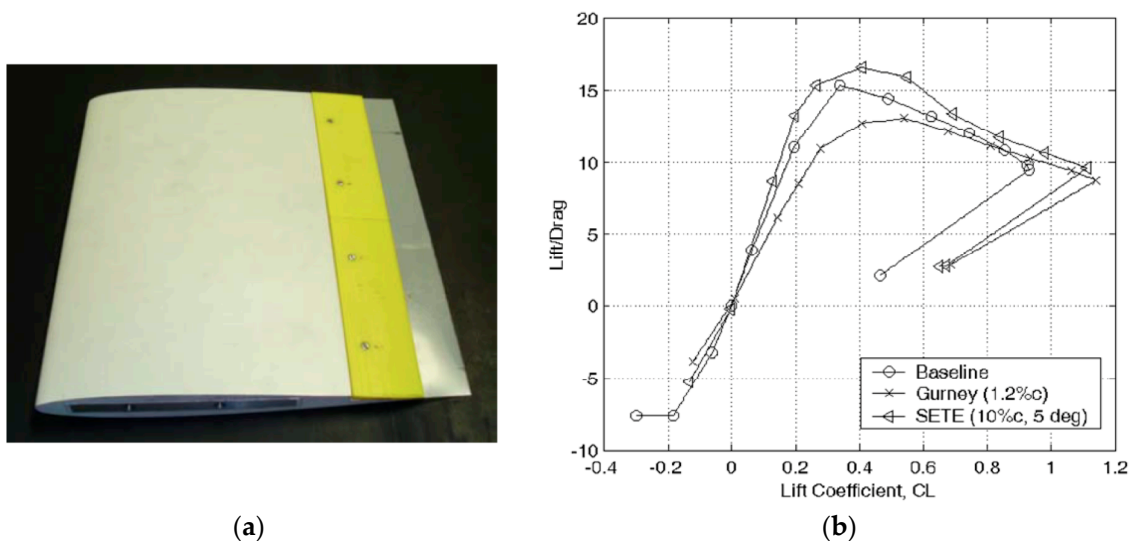


Figure 2. (a) NACA 0012 wing with static extended trailing edge (TE). (b) Variation of the aerodynamic efficiency with the coefficient of lift for baseline, Gurney and static extended trailing edge (SETE) configurations. The SETE configuration yielded better aerodynamic efficiency than the Gurney flap (adapted from Lui et al. [13]).

Background research indicates that extended trailing edges could be effective in reducing drag and increasing lift in wings, and TE extensions could lead to drag reduction and control flutter speed,

and could possibly act as control surfaces. A major disadvantage of TE extension is that it contributes to the overall weight of the aircraft. This research explores the use of segmented TE extensions as a means to increase aerodynamic efficiency and reduce the turbulent fluctuations in the wake of the wing.

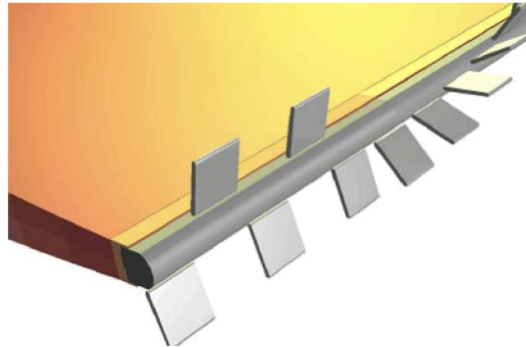


Figure 3. Array of Miniature Trailing Edge Effectors (MiTEs) (adapted from Lee and Kroo [14]).

2. Experimental Setup

2.1. Wind Tunnel

All the experiments were conducted at the University of Dayton Low Speed Wind Tunnel (UD-LSWT). The UD-LSWT has a 16:1 contraction ratio, 6 anti-turbulence screens and 4 interchangeable $76.2 \text{ cm} \times 76.2 \text{ cm} \times 243.8 \text{ cm}$ ($30'' \times 30'' \times 96''$) test sections. The test section is convertible from a closed jet configuration to an open jet configuration with the freestream range of 6.7 m/s (20 ft/s) to 40 m/s (140 ft/s) at a freestream turbulence intensity below 0.1% measured by a hot-wire anemometer. All the experiments mentioned in this paper were done in the open jet configuration, where an inlet of $76.2 \text{ cm} \times 76.2 \text{ cm}$ opens to a pressure sealed plenum. The effective length of the test section in the open jet configuration is 182 cm (72"). A $137 \text{ cm} \times 137 \text{ cm}$ ($44'' \times 44''$) collector collects the expanded air on its return to the diffuser. A photo of the UD-LSWT open jet configuration is shown in Figure 4. The velocity variation for a given RPM of the wind tunnel fan is found using a Pitot tube connected to an Omega (Norwalk, CT, USA) differential pressure transducer (Range: 0–6.9 kPa).

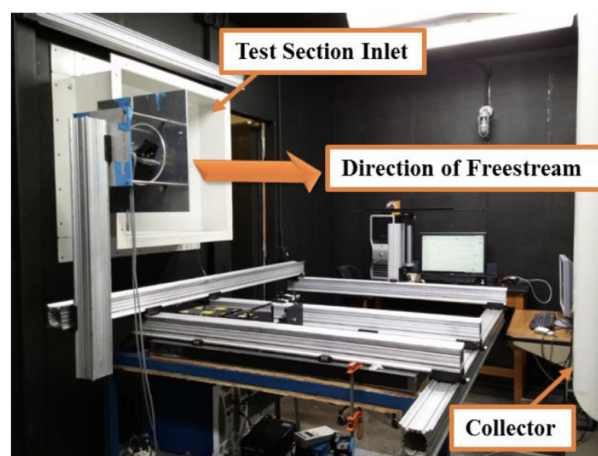


Figure 4. University of Dayton Low-Speed Wind Tunnel (UD-LSWT) in the open-jet configuration.

2.2. Test Model

A NACA 0012 semi-span wing with a 20.32 cm span (b) and a 10.16 cm chord (c) was designed in SolidWorks with the capability to attach multiple TE extensions, as seen in Figure 5. The wing was then 3D printed using Stratasys (Eden Prairie, MN, USA) uPrint SE Plus printer at the University of Dayton. The wing model uses two pieces to clamp the TE extensions to the main wing. The design allows for multiple TE extensions to be mounted. Seven segmented plexiglass TE extensions with thickness (t) of 1 mm, length (l) of 2.54 cm ($l/c = 0.25$) and a width (d) of 0.635 cm ($d/c = 0.0625$) were used. With the trailing edge extensions, the surface area of the wing was increased by 11% when compared to the baseline.

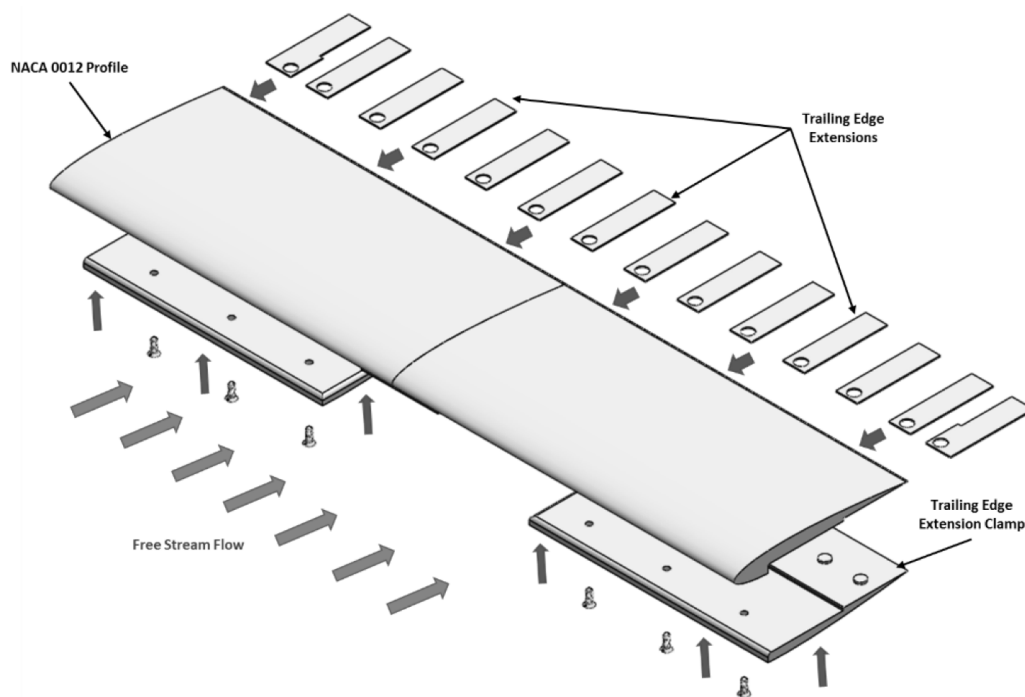


Figure 5. SolidWorks model of the AR 4 NACA 0012 wing with trailing edge (TE) extensions.

2.3. Force Based Experiment

Force based experiments were performed on the NACA 0012 semispan model with and without the segmented TE extensions at a Reynolds number of 200,000 (Test Matrix shown in Table 1). The models were tested at an angle of attack ranging from -15° to $+15^\circ$. Two trials of the same experiment were done while increasing and decreasing the angle of attack to check for hysteresis. The schematic of the force based test setup is shown in Figure 6.

Table 1. Test Matrix for the force based experiments.

Test Model	Reynolds Number	Angle of Attack (Degrees)
AR 4 NACA 0012 without TE Extensions	200,000	-15 to 15
AR 4 NACA 0012 with TE Extensions	200,000	-15 to 15

An ATI (Apex, NC, USA) Mini-40 force transducer was secured underneath the wing at the quarter chord location which interfaced with the Griffin motion rotary stage to change the angle of attack. The rotary stage was controlled using the Galil motion (Rocklin, CA, USA) software. The schematic of

the test setup is shown in Figure 6. The root of the wing was made to be in alignment with the splitter plate.

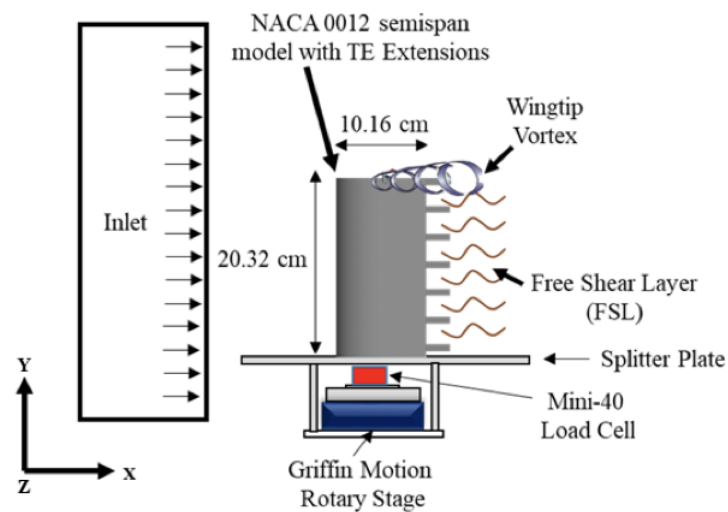


Figure 6. Schematic of the force based experiment test setup for the NACA 0012 semispan model with TE extensions. A similar setup was used for the NACA 0012 wing without TE extensions, as well.

2.4. Force Transducer

An ATI Industrial Automation Mini-40 (www.ati-ia.com) sensor was used to determine the wing lift and drag coefficients. The specifications for the Mini-40 sensor are shown in Table 2. The normal and axial force was measured using the X and Y axes of the sensor. The sampling rate during data acquisition from the Mini-40 was 100 Hz. To make sure the sampling rate doesn't bias the force based experiments due to vortex shedding frequency, force experiments were conducted at the Reynolds number of 135,000 and 200,000, and the lift coefficient variation was compared. Tare values were taken before and after each test, and then the average of the two tares are subtracted from the normal and axial force readings.

Table 2. Test Matrix for the force based experiments.

	F_X (N)	F_Y (N)	F_Z (N)	T_X (Nm)	T_Y (Nm)	T_Z (Nm)
Range	40	40	120	2	2	2
Resolution	1/100	1/100	1/50	1/4000	1/4000	1/4000

2.5. Particle Image Velocimetry (PIV) Setup

Streamwise Particle Image Velocimetry (PIV) was conducted in the free shear layer of the NACA 0012 wall-to-wall model with and without the segmented TE extensions. Two end plates were installed at the wingtips to prevent the rollup of wingtip vortices and the reduction of three dimensionality. The PIV measurements were obtained using a Vicount smoke seeder with glycerin oil and a 200 mJ/pulse Nd: YAG frequency doubled laser Quantel Twins CFR 300 (Bozeman, MT, USA). A Cooke Corporation (Romulus, MI, USA) PCO 1600 camera (1600 × 1200 pixel array) with a 105 mm Nikon (Tokyo, Japan) lens was used to capture the images. One plano-convex lens and one plano-concave lens were used in series to convert the laser beam into a sheet. The laser and the camera were triggered simultaneously by a Quantum composer (Bozeman, MT, USA) pulse generator. In each test case, over 1000 image pairs were obtained and processed using Innovative Scientific Solution Inc. (ISSI) (Dayton, OH, USA) Digital Particle Image Velocimetry (DPIV) software. A total

of two iterations were performed during PIV processing with 64-pixel interrogation windows in the first iteration and 32-pixel interrogation windows in the second iteration. Both the streamwise and cross-stream PIV interrogations were conducted with a Reynolds number of 135,000. The test matrix for the PIV experiment is shown in Table 3. The schematic of the PIV test setup is shown in Figure 7a. The uncertainty of the velocity measurements from the PIV setup was calculated to be 0.1 m/s.

Table 3. Test Matrix for Free Shear Layer (FSL) Particle Image Velocimetry (PIV) interrogation.

Test Model	Angle of Attack (Degrees)	Interrogation Location
AR 4 NACA 0012 without TE Extensions	0, 2, 4, 6, 8	Behind TE
AR 4 NACA 0012 with TE Extensions	0, 2, 4, 6, 8	Behind TE Extension

In the baseline case, the interrogation window was placed near the trailing edge of the wing, as shown in Figure 7b, to determine the vortex shedding and the momentum deficit. In the wing with the segmented TE extensions, the interrogation window was placed at the trailing edge of the TE extension as shown in Figure 7a,c. A Nikon 105 mm lens was used in the streamwise PIV case, which gave a spatial resolution of 292 pix/cm in both axes. The size of the field of view was 5.5 cm × 4.1 cm which gave a magnification factor of 0.21. The δT for the images were set to obtain an average particle displacement of 8–10 pixels in the wake of the wing.

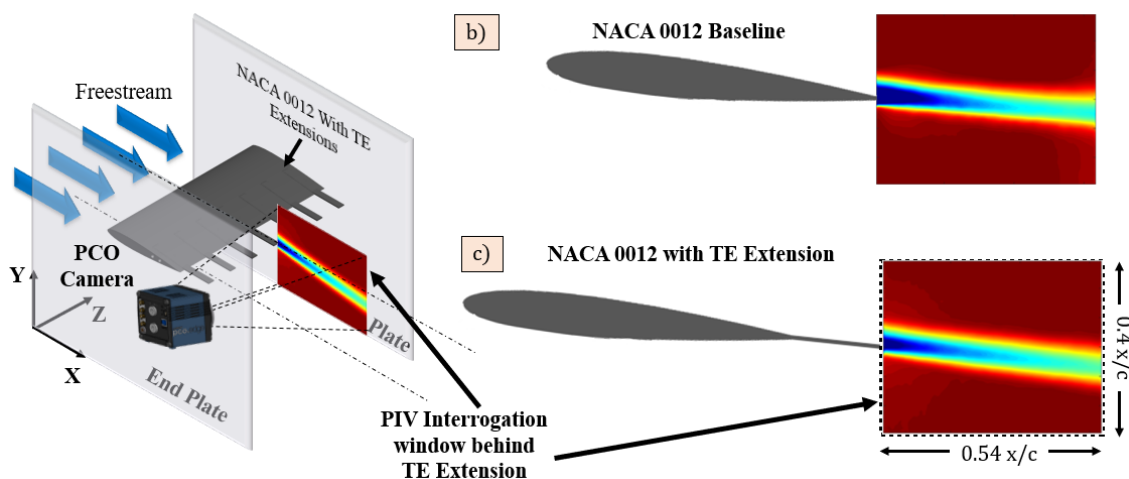


Figure 7. (a) Schematic of the PIV test setup for the NACA 0012 wing with TE extensions. A similar setup is used for the baseline wing. The PIV interrogation window for (b) the baseline case was located at the TE and (c) for the wing with the TE extension, it was location at the trailing edge of the TE.

3. Influence of Reynolds Number

Since the Reynolds numbers chosen for this study (200,000 and 135,000) fall within the sub-critical and transitional regime, the influence of viscous effects on the aerodynamic coefficients must be quantified. Spedding and McArthur [15] found a functional relationship between the lift curve slope and the Reynolds number between the order of 10^4 and 10^5 as $C_L = 2\pi Re^\beta$, where β exponents have the value of 0.19 for a 2D airfoil. However, the Reynolds number influence of the coefficient of lift in the moderate Reynolds numbers between 100,000 and 600,000 is less explored experimentally.

The viscous effects on the aerodynamic coefficients can be determined through viscous XFOIL simulation. Figure 8 shows the coefficients of lift and drag obtained from viscous flow simulation in XFOIL for the NACA 0012 at the two Reynolds numbers considered in this study. The lift coefficient deviates from the theoretical 2π prediction at all angles of attack. This deviation is traced to the movement of the separation point from the trailing edge of the airfoil and the formation of a laminar

separation bubble. DNS simulations at a Reynolds number of 50,000 from I.Rodríguez et al. [16] showed the presence of a laminar separation bubble and the vortex breakdown at the end of the bubble because of the Kelvin-Helmholtz mechanism. The separation point moves towards the leading edge with increased angle of attack. The departure of the lift curve slope from the inviscid theory can be quantified through the lift curve slope as shown in Figure 9.

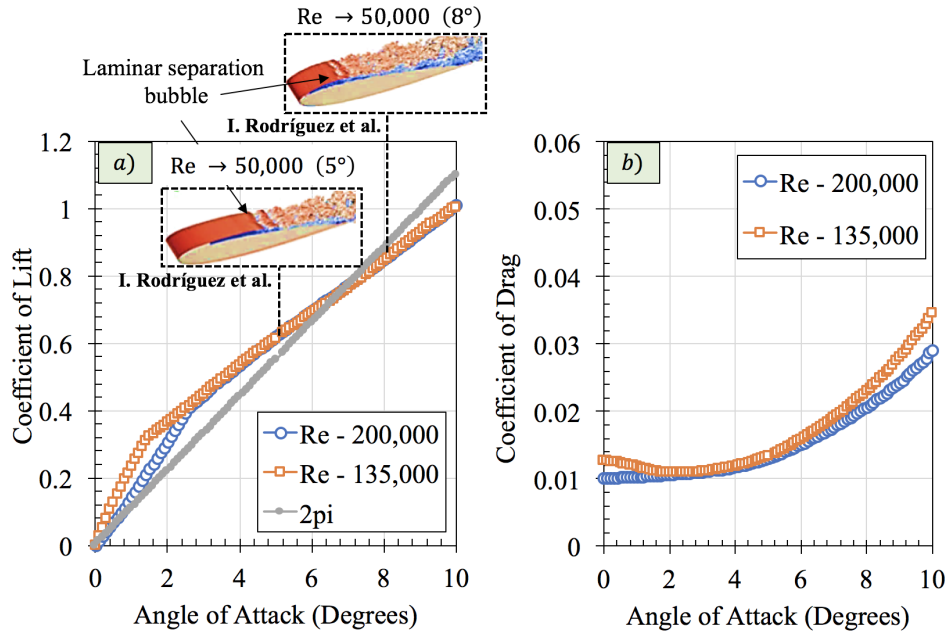


Figure 8. Comparison of (a) lift coefficient (b) drag coefficient at different Reynolds numbers.

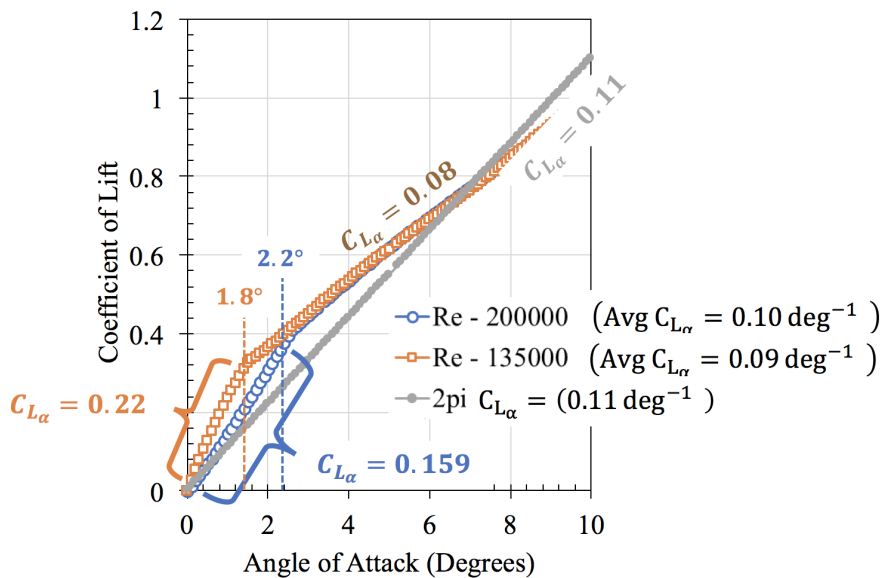


Figure 9. Comparison of lift coefficient at different Reynolds numbers.

There is a change in the lift curve slope around 2° angle of attack for both the Reynolds number cases, but at angles of attack greater than 2°, the lift curve slope ($C_{L\alpha}$) stays constant at 0.08 deg^{-1} . On an average, the entire lift curve slope of the NACA 0012 at a Reynolds number of 135,000 is around 0.09 deg^{-1} , and at a Reynolds number of 200,000 it is around 0.1 deg^{-1} , which deviate from the

lift curve slope of 2π by 18% and 9%, respectively. Irrespective of the viscous effects, the lift curve remains linear, and with the relatively smaller percent difference between the theoretical and simulated lift curve slope, the relationship between induced drag and the lift coefficient is expected to remain the same.

Even though different Reynolds numbers were used for force-based testing and PIV, the lift and drag characteristics of the NACA 0012 are the same as evidenced from the simulated results shown in Figure 9. After 2° angle of attack, the lift coefficient from the two different Reynolds numbers is identical. The drag coefficient also shows similar behavior and magnitude at two different Reynolds numbers as well. Therefore, it can be concluded that there are no significant changes in the flow characteristics over the NACA 0012 at the two different Reynolds numbers considered for this study.

4. Results

4.1. Force-Based Experimental Results

The coefficient of lift variation with angle of attack is shown in Figure 10 for the Reynolds number of 200,000 for both the baseline case and the wing with TE extensions. The coefficient of lift variation is compared with the theoretical lift coefficient variation given by McCormick's formula (McCormick [17]). According to McCormick's formula, the lift curve slope depends on the aspect ratio by

$$a = \frac{dC_L}{d\alpha} = a_0 \left(\frac{AR}{AR + 2 \left(\frac{AR+4}{AR+2} \right)} \right) \quad (1)$$

where $a_0 = 2\pi$, according to thin airfoil theory, and AR is the aspect ratio of the wing. The best fit line of the lift curve gives an effective aspect ratio of two, which is smaller than the intended aspect ratio of four. The reduction in effective aspect ratio could be due to the wing-splitter plate interface contributing to the three dimensionality of the flow. The baseline results shows a good match with the results from Ngo and Barlow [18] for a Reynolds number of 480,000 for Aspect ratio (AR) 2. The added 11% surface area was taken into account in the calculation of lift from the wing with the TE extensions case. The comparison of lift coefficient magnitude between the baseline and the wing with TE extensions shows almost no variations as a function of angle of attack. Any changes in lift coefficient falls between the uncertainty band of the sensor, as indicated by the error bars.

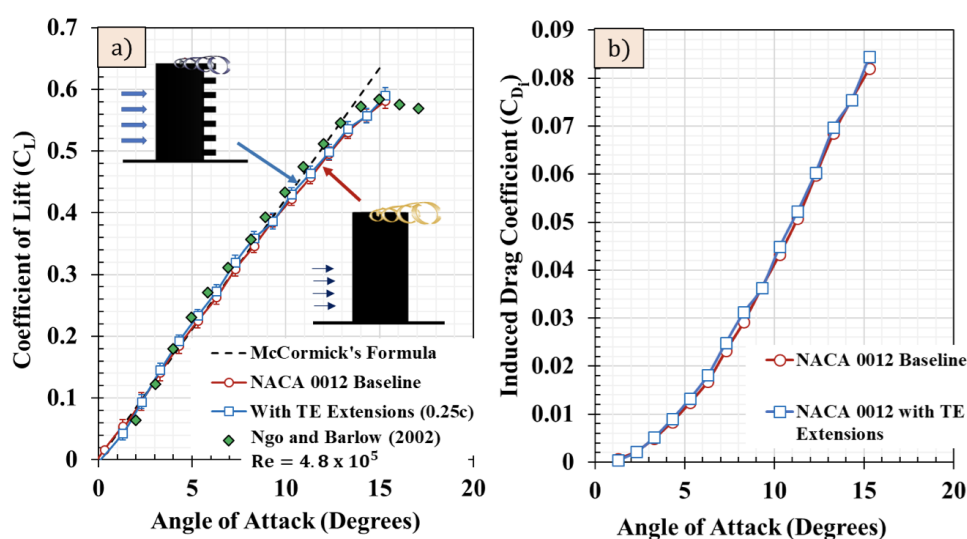


Figure 10. (a) Variation of Coefficient of Lift with angle of attack for the baseline wing and the wing with TE extensions. The lift curve slope shows similar variation with negligible differences between the two cases; (b) Variation of the coefficient of induced drag for both cases.

The differences in lift is used to calculate the differences in the induced drag. The induced drag was found by

$$C_{D\text{Induced}} = \frac{C_L^2}{\pi e AR} \quad (2)$$

where e is the span efficiency and AR is the aspect ratio. The span efficiency of the baseline and wing with TE extensions was found using the lift curve slope equation from thin airfoil theory (Equation (3)).

$$a = \frac{a_0}{1 + \frac{a_0}{\pi e AR}} \quad (3)$$

where a is the lift curve slope of the finite wing and $a_0 = 2\pi$. From Equation (3), the span efficiency for the baseline was 0.69 for both the cases, since they have the same lift curve slope. The wing with TE extensions shows a higher induced drag coefficient across all angles of attack (Figure 10b). At a 14° angle of attack, the induced drag shows a 6% increase in the wing with TE extensions when compared to the baseline. At lower angles of attack, the differences in the induced drag between two cases are not resolvable, due to the uncertainty limit of the ATI mini-40 sensor. Because drag is an order of magnitude less than the lift, the sensor was not capable of measuring the differences in the drag forces between the two cases. Therefore, streamwise Particle Image Velocimetry (PIV) was used to determine the momentum deficit and the parasitic drag of the wing configurations. The results from the PIV are discussed in the section below.

4.2. Momentum Deficit

The streamwise velocity U_x contour obtained behind the TE extension and behind the trailing edge of the baseline wing is shown in Figure 11a. The momentum deficit increases with an increase in angle of attack, as expected for the both cases. However, subtle differences can be observed in the momentum deficit between the two cases. At a 2° angle of attack, the momentum deficit behind the TE extension is greater than the momentum deficit behind the trailing edge of the wing. This could be due to increased skin friction drag due to the presence of the TE extension. As the angle of attack increases, a different trend is observed. At the 4° and 6° angle of attack cases, the differences between the two cases are hard to observe since the contours look almost similar. However, at an 8° angle of attack, a lower momentum deficit can be observed behind the TE extension when compared to the baseline. This shows that the TE extension reduced the pressure drag of the wing.

These observations are more apparent in the momentum deficit profiles shown in Figure 11b. The profiles were taken by averaging 10 data columns in the center of the field of view, as highlighted in Figure 11. This region was chosen to avoid any influence of the distortion and spherical aberration in the corners of the field of view. The normalized streamwise velocity is plotted against the normalized wake-half width y/L_0 , where L_0 is the wake half-width which is considered as the location of 99% U_∞ . The profiles indicate that the momentum deficit at 2° and 4° angles of attack between the two cases are similar. At 6° and 8° angles of attack, however, clear differences between the two cases can be seen. The momentum deficit behind the TE extension is clearly lower than the baseline. The momentum deficit profiles shown in Figure 11b was used to determine the total parasitic drag coefficient of the baseline NACA 0012 wing and the wing with TE extensions. The total parasitic drag coefficient of the wing was found by integrating the sectional drag coefficient along the wingspan. The sectional drag coefficient behind the trailing edge and the TE extension was determined by the momentum deficit equation,

$$C_D = \frac{\rho U_\infty^2}{q_\infty S} \int \frac{U_x}{U_\infty} \left(1 - \frac{U_x}{U_\infty}\right) dy \quad (4)$$

where ρ is the density, U_∞ is the freestream velocity, q_∞ is the dynamic pressure, U_x is the streamwise velocity and S is the surface area of the wing. The momentum deficit equation represents the loss of momentum in the wake due to the presence of the wing in the flow. According to Newton's second

law, by determining the reduction in the freestream momentum due to the presence of the wing, the total drag of the wing can be estimated. The derivation of the momentum deficit principle is detailed in Anderson [19]. The drag coefficient variation with angle of attack is shown in Figure 12. As expected, the drag coefficient behind the trailing edge varies non-linearly with the angle of attack for both cases. The magnitude of the drag coefficient behind the TE extension is lower than the baseline at all angles of attack. Even though the momentum deficit profiles in Figure 11b look similar for both the cases at lower angles of attack, the TE extension case has a higher chord length and surface area when compared to the baseline case. Therefore, for a similar normalized momentum deficit profile, the coefficient of drag is lower in the wake behind the TE extension.

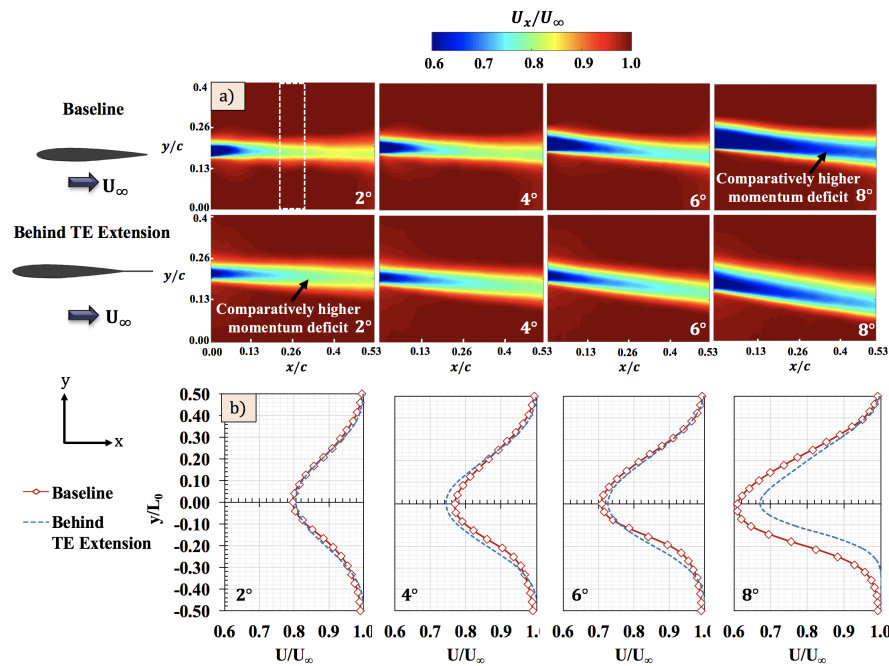


Figure 11. (a) Streamwise velocity contours in FSL behind the trailing edge of the NACA 0012 wing and behind the TE extension (b) Momentum deficit profiles at different angles of attack for both cases. The momentum deficit behind the TE extension is lower at higher angles of attack when compared to the baseline.

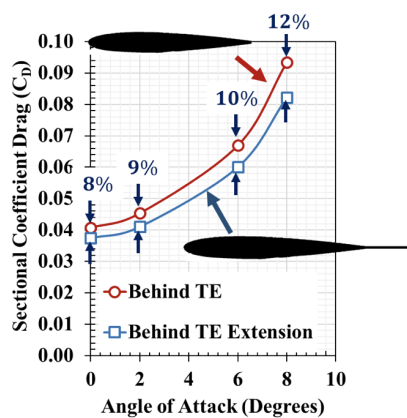


Figure 12. Variation of coefficient drag estimation behind the trailing edge and behind the TE extension as a function of angle of attack. The estimated drag coefficient behind the TE extension is lower than the drag coefficient behind the hole.

The differences in the sectional coefficient of drag increases with an increase in angle of attack from 8% at 42° to 12% at 8° . To determine the total parasitic drag coefficient of the entire wing with and without TE extensions, a theoretical distribution of the sectional drag coefficient is plotted in Figure 13 for the 8-hole wing using the drag coefficient values obtained from the momentum integral. The sections of the wing with the TE extension has a lower drag coefficient than the trailing edge as observed in Figure 12. The theoretical drag coefficient distribution increases with angle of attack, as expected.

The total drag coefficient of the wing was found by integrating the sectional drag coefficient along the span of the wing. The net parasitic drag coefficient of the NACA 0012 baseline wing and the wing with TE extensions are shown in Figure 14a for multiple angles of attack. The total parasite drag of the wing with TE extensions is lower than the NACA 0012 baseline wing across all angles of attack. Adding the induced drag found from force based experiment and parasitic drag data found from PIV, the total drag coefficient for the baseline and the wing with TE extensions is shown in Figure 14b. The total drag for the wing with TE extensions is also lower when compared to the baseline at all angles of attack. Since the induced drag remained the same for both the cases (Figure 10b), the total drag shows the same trend as the parasitic drag coefficient. Total drag reduction in the order of 8% is observed at an angle of attack of 0° , increasing to 9% at an 8° angle of attack. The average reduction in the drag coefficient due to the TE extensions is around 8%. This result indicates that the TE extensions are effective at all angles of attack.

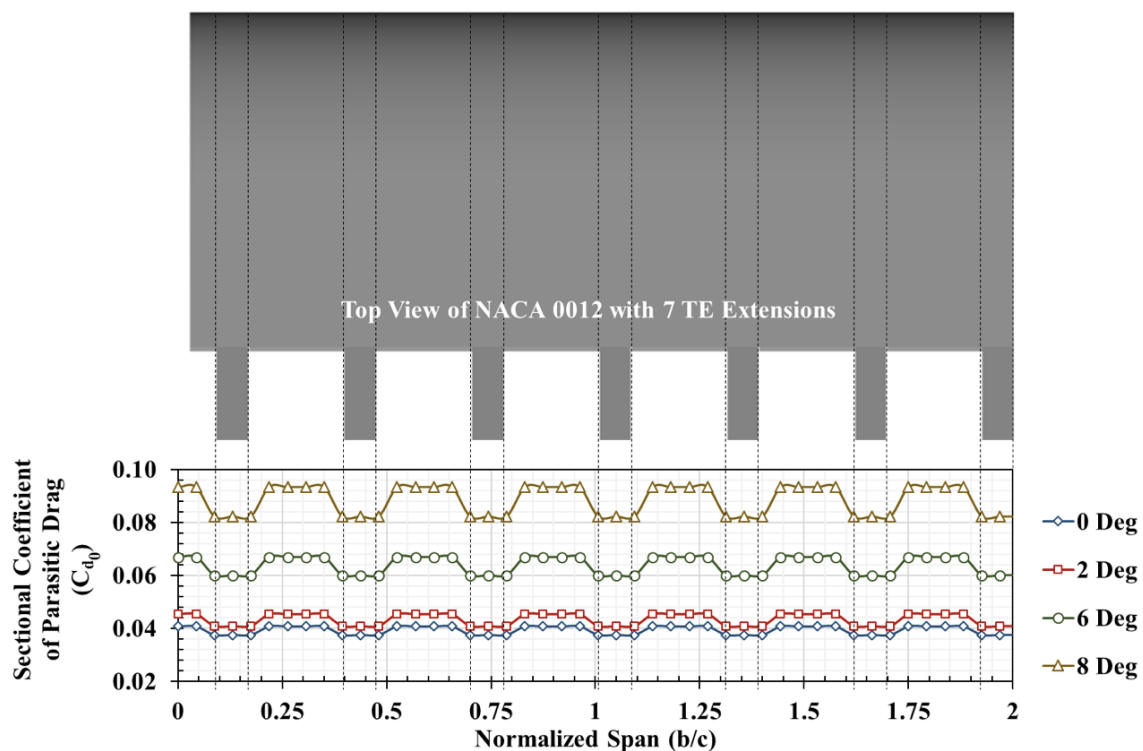


Figure 13. Section drag coefficient variation across the span for wing with seven TE extensions. The drag coefficient behind the TE extension is lower than the drag coefficient behind the trailing edge of NACA 0012.

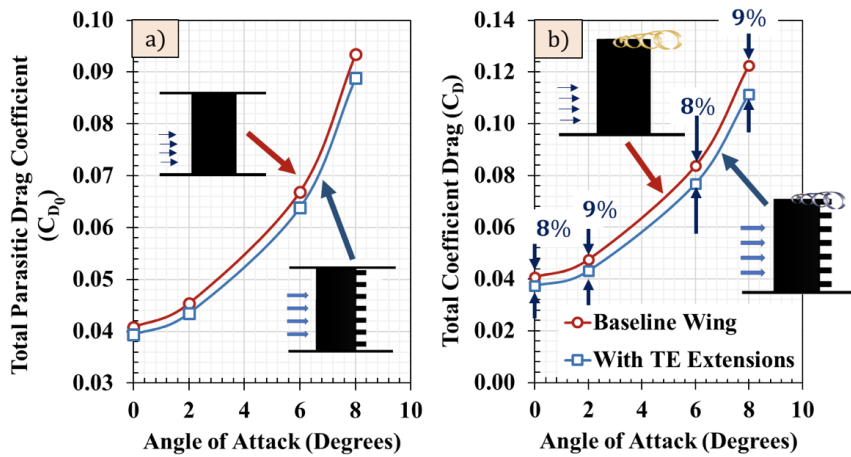


Figure 14. Variation of (a) net parasitic drag coefficient and (b) the total drag coefficient of the baseline wing and wing with TE extensions. The wing with TE extensions shows an average decrease in the drag coefficient around 8%.

4.3. Z-Vorticity

The Z-vorticity contours and profiles behind the wake of the baseline NACA 0012 wing and with the TE extensions can be seen in Figure 15a,b. The Y-vorticity in the wake was determined by

$$\omega_z = \left(\frac{\partial v}{\partial x} - \frac{\partial u}{\partial y} \right) \tag{5}$$

The velocity gradients in Equation (5) were determined by the central difference technique using the experimental velocity data.

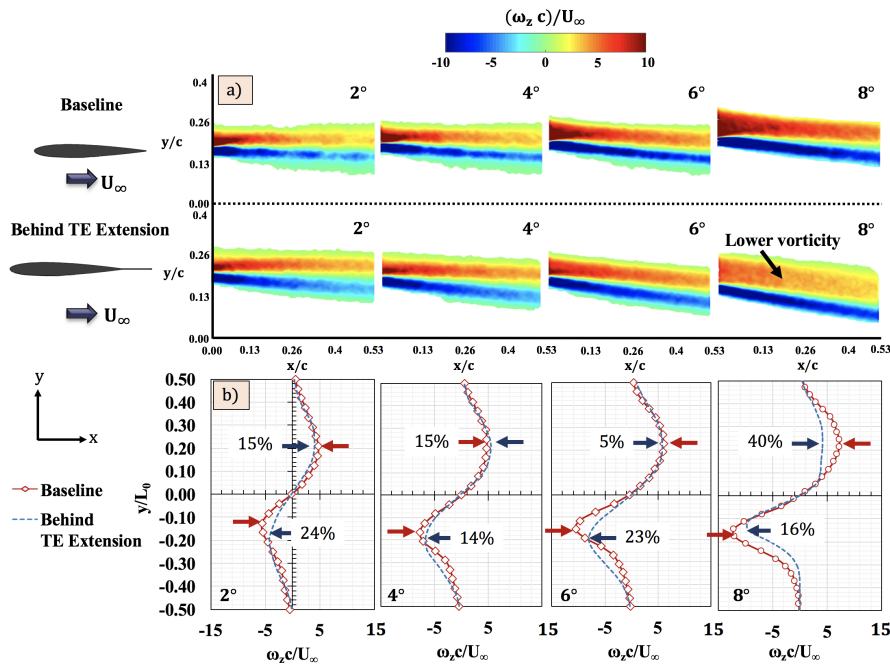


Figure 15. (a) Z-vorticity contours in FSL behind the trailing edge of the NACA 0012 wing and behind the TE extension (b) Vorticity profiles at different angles of attack for both cases. The local rotating velocity behind the TE extension is lower at higher and lower angles of attack when compared to the baseline.

Similar magnitudes between the two cases are observed in the vorticity contours at lower angles of attack. However, at an 8° angle of attack, a lower vorticity magnitude is observed behind the TE extension. The vorticity profiles across the contours are compared between the two cases in Figure 15b. At a 2° angle of attack, a reduction in vorticity of 15% on the top surface and 24% on the bottom surface was observed with TE extensions. Then, at a 4° angle of attack, the difference in peak vorticity decreased. The top surface vorticity had a 15% increase and the bottom had a 14% decrease with TE extensions. However, at an 8° angle of attack, the extensions reduce the peak vorticity strength by 40% in the top surface and 16% on the bottom. This shows that the TE extensions are most effective at higher angles of attack, as the pressure drag begins to dominate over skin friction drag. The reduced vorticity at an 8° angle of attack also indicates changes in the vortex shedding, which is discussed in the next section. The reduction in vorticity also indicates a reduction in total pressure loss through Crocco's theorem, which in turn reduces drag.

4.4. Coherent Structures

As seen in the literature review section, vortex shedding frequency and turbulent length scales contribute to turbulence-induced pressure fluctuations, sound generation and structural vibrations. The effect of the TE extensions on vortex shedding frequency and turbulent length scales can be determined by comparing the changes in the coherent structures present in the wake between the baseline wing and wing with TE extensions. The coherent structures can be determined by performing a two-point correlation of fluctuating velocities (u' and v') in the wake. The two-point correlation also allows determination of the length scales associated with the coherent turbulent motions. Bendat and Piersol [20] defined the two-point correlation as

$$\rho_{u_i u_j} = \frac{u'_i(X_1, t) * u'_j(X_2, t + \tau)}{\sqrt{u'_i(X_1)^2} \sqrt{u'_j(X_2)^2}} \quad (6)$$

where X_1 and X_2 are two spatial locations in the PIV field of view, τ is the time delay (which is chosen to be zero for the results shown below), u' represents the fluctuating velocities in the i and j directions and $\rho_{u_i u_j}$ is the correlation coefficient. Figures 16 and 17 show the contour levels of the normalized two-point correlation functions with zero time delay of the streamwise (u) and transverse (v) fluctuating velocities, respectively, for 2° , 4° , 6° , and 8° angles of attack in the wake of the baseline wing and in the wake of the TE extension. In each case, the reference point (X_1) is chosen to be at the center of the upper shear layer, which is also the upper surface boundary layer at the trailing edge, as indicated in Figure 16.

The intent behind the correlation is to highlight the correlation in velocity fluctuations between the upper surface boundary layer and the near wake. The $\rho_{u_i u_j}$ contour images for the baseline case shows extensive coherent structures of alternating positive and negative correlation values. Specifically, spatially alternating regions of positive and negative correlation are indicative of the spatially and temporally periodic motions of the fluid. These motions can be related to the tonal character of fluctuations in the flowfield at the frequency of vortex shedding. In the baseline case, the coherent structures are well formed in the shear layer emanating from the upper and lower surface of the wing. The magnitude of correlations is also higher when compared to the upper surface shear layer. As the angle of attack increases, the length scales (represented by the horizontal distance of each coherent structure) decrease due to an increased vortex shedding frequency. This can be observed by quantifying the number of coherent structures in the wake. At a 2° angle of attack, there are eight coherent structures, and at an 8° angle of attack, there are ten coherent structures. However, in the wake of the TE extension, the correlation of the upper surface shear layer and the near wake is significantly lower when compared to the baseline case. This indicates comparatively weaker vortex shedding and turbulent fluctuations in the wake of the TE extension. It is interesting to note that with the increase in the downstream distance, the correlation of the velocity fluctuations in the TE extension

case almost goes to zero at all angles of attack. The reason why there is a diminishing correlation along the streamwise direction in the TE extension case could be due to the mitigation of vortex shedding by the TE extension. The TE extension reduces the recirculation behind the trailing edge of the wing by acting as a physical barrier, similar to the function of splitter plates in the trailing edge of cylinders. Therefore, lower vortex shedding leads to lower correlation between the wake and the upper shear layer. This reduction in vortex shedding by the TE extension is also seen in vorticity plots in Figure 15. However, in the baseline case, there is a strong correlation across the field of view.

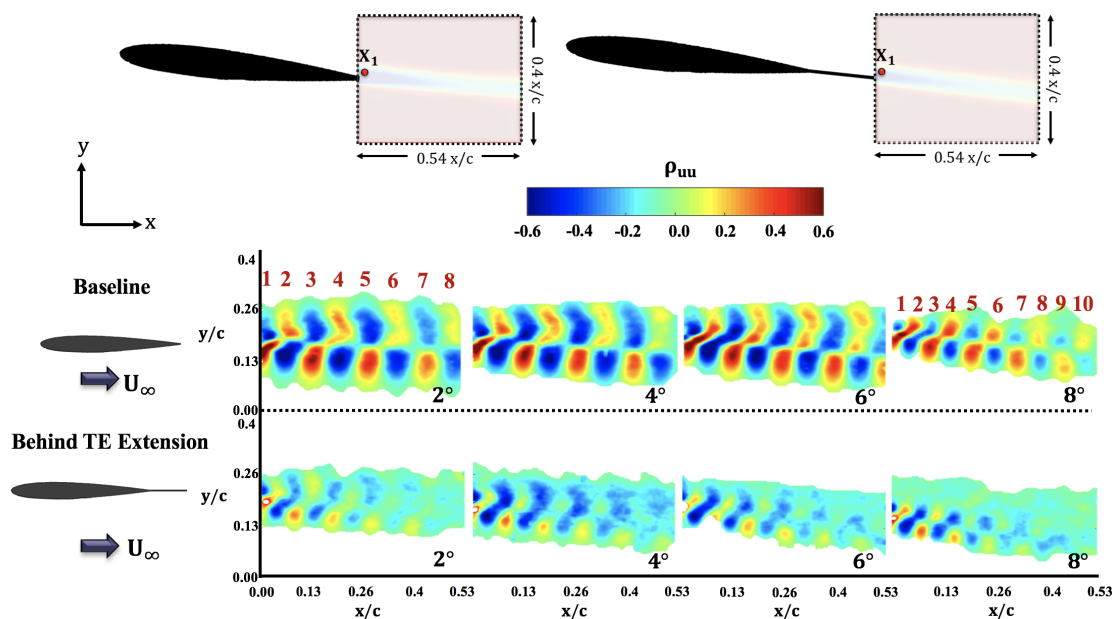


Figure 16. Contours of two-point correlations of the streamwise velocity component for the baseline wing and for the wing with TE extensions. Weaker correlations are observed in the wake behind the TE extension, indicating lower length scales and velocity fluctuations.

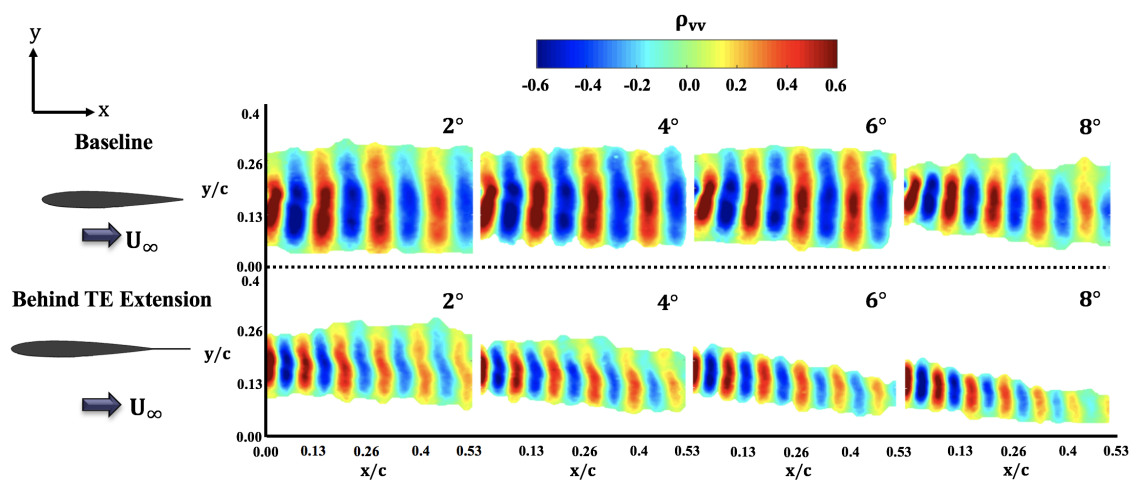


Figure 17. Contours of two-point correlation of the transverse velocity component for the baseline wing and for the wing with TE extensions. Similar to $\rho_{u_i u_j}$, weaker correlations are observed in the wake behind the TE extension lower velocity fluctuations. Also, the decrease in wavelength of the correlation indicates a decrease in turbulent length scales.

Similar behavior is observed in the ρ_{vv} (transverse) velocity correlations in the wake of the baseline wing and in the wake of the TE extension. The large alternating regions of positive and negative

correlation appear in the baseline and the TE extension cases, but the wavelength of the correlations in the TE extension is almost of half of that of the baseline wing. The reduction in length scales indicate lower velocity fluctuations in the wake of the TE extension, which results in lower pressure fluctuations and lower drag as observed in Figure 14b. The decrease in turbulent length scales increases the viscous dissipation rate which results in lower velocity and pressure fluctuations, and hence lower drag. The reduced fluctuations in the TE extension case can also be seen in the RMS quantities of the streamwise and transverse velocities.

4.5. Reynolds Stress

The Reynolds stress components are indicative of the turbulent intensity within a developing shear layer. Mohsen [21] suggested that the local maximum Reynolds stress $(u'v')_{max}$ in the Reynolds stress profile may be correlated to the large pressure fluctuations. Therefore, the Reynolds stress distribution in the wake are of great interest as they can indicate how TE extensions affect the amount of turbulence in the flow. The contour plots and profiles of the Reynolds stress comparing the NACA 0012 baseline wing and with TE extensions can be seen in Figure 18a,b.

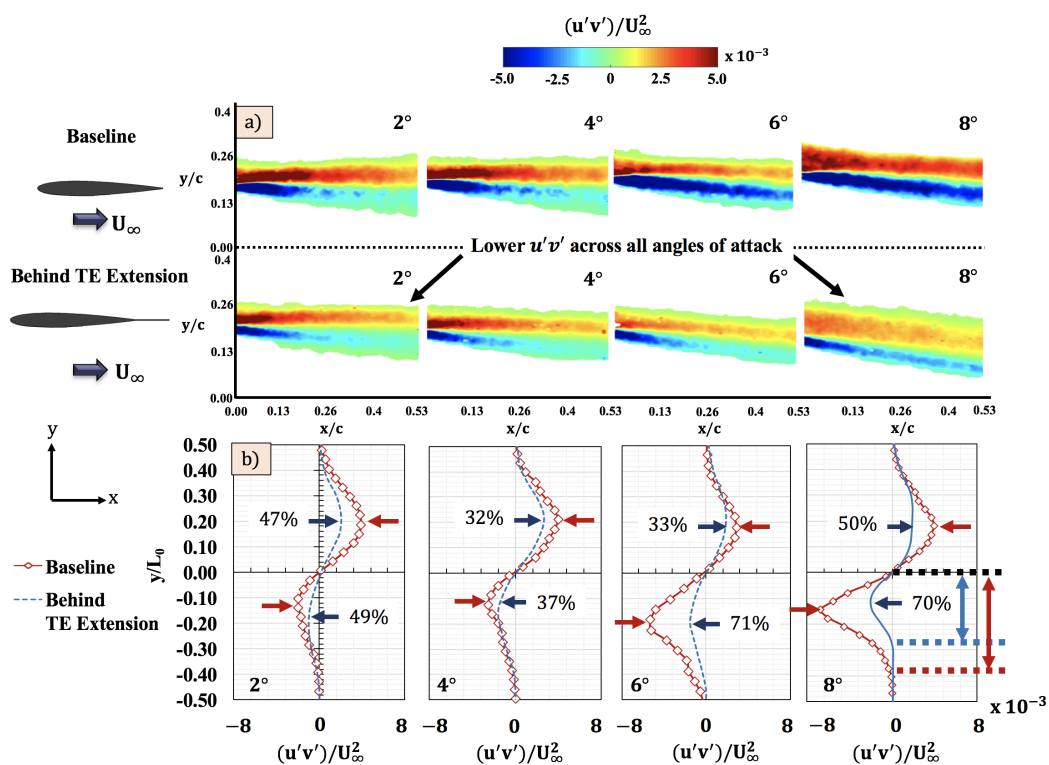


Figure 18. (a) Streamwise Reynolds stress contours in FSL behind the trailing edge of the NACA 0012 wing and behind the TE extension (b) Reynolds stress profiles at different angles of attack for both cases. The Reynolds stress behind the TE extension is lower across all angles of attack when compared to the baseline.

The magnitude of the both the upper and lower surface Reynolds stress behind the TE extension is lower than the baseline case at all angles of attack. The lower Reynolds stress magnitude behind the TE extension might indicate that the turbulent fluctuations emanating from the upper and lower surface boundary layer has reduced drastically when compared to the baseline. However, a thorough investigation of this would require performing PIV on the boundary layer itself. In both the cases, the Reynolds stress varies in the streamwise direction, but the changes in the streamwise direction in the Reynolds stress is greater in the baseline case when compared to the TE extension case. This trend can be clearly seen at an 8° angle of attack. A uniform variation in the Reynolds stress can be observed

behind the extended TE case, where the Reynolds stress decreases with an increase in downstream distance behind the trailing edge of the baseline wing. The differences in the Reynolds stress between the two cases can be seen clearly in the profiles shown in Figure 18b. Surprisingly, the magnitude of the Reynolds stress in the upper surface is lower than the magnitude of the Reynolds stress in the lower surface in both cases, but the magnitude of the Reynolds stress in both the upper and lower surface of the TE extension case is lower than the baseline in all angles of attack. The Reynolds stress is lowered by 47% and 49% on the upper and lower surfaces respectively at 2° with the TE extensions. The peak Reynolds stress differences then decreases to 32% and 37% at a 4° angle of attack with extensions, and again greatly increase at higher angles of attack. This displays a trend similar to the vorticity profiles. At 8° the peak Reynolds stress with the TE extensions is 50% lower on the upper surface and 70% on the lower surfaces. It is interesting to note that the TE extension affects the Reynolds stress in the lower surface more significantly than the upper surface.

4.6. Root-Mean Square (RMS) Velocities

The root mean square of U and V velocities were determined by

$$U_{RMS} = \sqrt{(u'_x)^2} \tag{7}$$

$$V_{RMS} = \sqrt{(v'_y)^2} \tag{8}$$

where u'_x is the fluctuating velocity about the x-axis, and v'_y is the fluctuating velocity about the y-axis. The freestream normalized U_{RMS} is shown in Figure 19 for both the baseline and the wing with TE extension. The magnitude of U_{RMS} increases with an increase in angle of attack for both baseline and the wing with TE extension. On comparison with the baseline case, the U_{RMS} behind the TE extension is reduced for all angle of attack cases. Therefore, the fluctuations in the U velocity are reduced significantly by the TE extension.

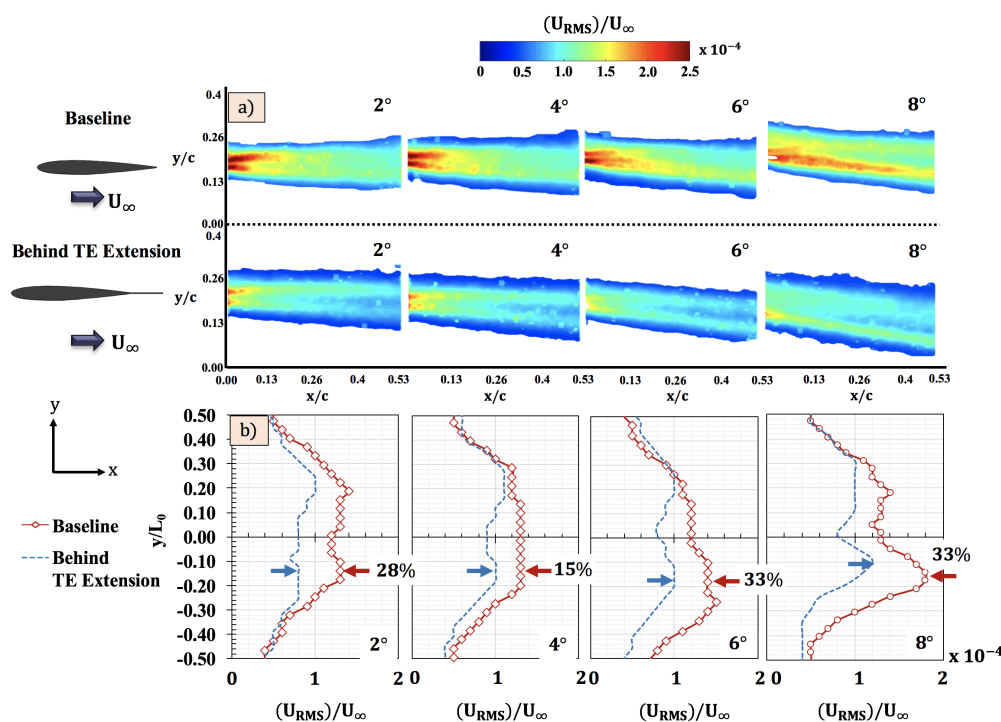


Figure 19. (a) Streamwise U_{RMS} contours in FSL behind the trailing edge of the NACA 0012 wing and behind the TE extension. (b) U_{RMS} profiles at different angles of attack for both cases. Large decreases were observed in the U_{RMS} of the TE extension.

In both cases and in all angles of attack, the U_{RMS} in the lower surface was found to be greater than the upper surface. This result correlates with the increase Reynolds stress in the lower surface when compared to the upper surface of the wing. The differences in the U_{RMS} can be seen clearly in the U_{RMS} profiles shown in Figure 19b. The average difference in the peak U_{RMS} behind the baseline wing and behind the TE extension is around 30%. Similar results are observed in V_{RMS} as well, which is shown in Figure 20a. The normalized V_{RMS} values of 1.8×10^{-5} and 2.0×10^{-5} are highlighted in white to distinctly observe the free shear layer. Similarly to the U_{RMS} , the magnitude of the V_{RMS} in the wake behind the TE extension is significantly reduced. The differences can also be clearly seen in the V_{RMS} profiles shown in Figure 20b. The peak differences in V_{RMS} profiles display consistent reductions with TE extensions at an average of 57%. The magnitude decrease in V_{RMS} is greater than the magnitude decrease in U_{RMS} in the wake behind the TE extension. A similar trend was seen in the coherent structures. The two-point correlation of the transverse velocity showed significant changes when compared to the streamwise velocity correlation. The reduction in the length scales might be the cause of lower fluctuations in the wake behind the TE extension.

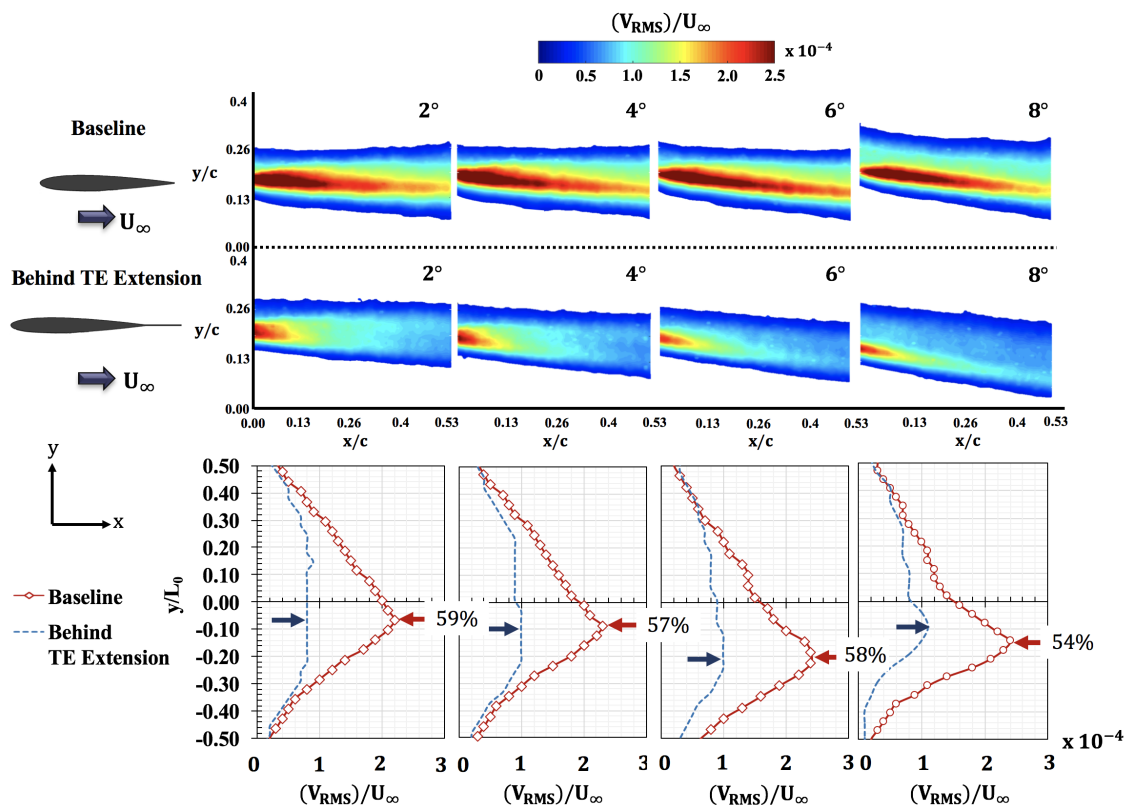


Figure 20. Streamwise V_{RMS} contours and profiles in FSL behind the trailing edge of the NACA 0012 wing and behind the TE extension at different angles of attack for both cases. Large decreases were observed in the V_{RMS} of the TE extension.

5. Conclusions

A NACA 0012 baseline semi-span wing model was tested with and without segmented trailing edge (TE) extensions. Force measurements and PIV experiments were conducted to analyze how the segmented TE extensions affected the vorticity and turbulent signatures in the wake. The prominent conclusions taken from the research are:

1. The TE extensions had a minor effect on the coefficient of lift but had measurable impact on the coefficient of drag at high angles of attack. With the segmented TE extensions, the total drag coefficient reduced by 8% at an 8° angle of attack.

2. Evidence for the cause of reduction in parasitic drag with TE extensions was supported by mean flow quantities, such as mean velocity and normalized vorticity. Both parameters showed measurable and significant reductions when compared to the baseline, especially in the vorticity case. The average reduction in vorticity is in the order of 40% at an 8° angle of attack.
3. The reduction in vorticity behind TE extensions was further supported by determining the coherent structures in the wake. A comparatively lower correlation of the wake and the upper surface shear layer indicates lower velocity and pressure fluctuations behind the TE extensions when compared to the baseline.
4. The lower pressure fluctuations can be supported by the changes observed in the Reynolds stress. On average, the magnitude of the Reynolds stress was reduced by 40% on the upper surface and by 55% on the lower surface.
5. The reduction in fluctuations are further validated by determining U_{RMS} and V_{RMS} , which showed an average decrease in magnitude of 15% and 57%, respectively.

These results provide evidence to consider segmented trailing edge extensions as a means to reduce turbulent fluctuations and vortex shedding in the wake of the wing without compromising on lift production.

Author Contributions: Conceptualization, S.G.; Data curation, S.G. and D.C.; Formal analysis, S.G.; Methodology, S.G.; Supervision, S.G.; Visualization, D.C.; Writing—original draft, D.C.; Writing—review & editing, S.G.

Funding: This research received no external funding.

Conflicts of Interest: The authors declare no conflict of interest.

References

1. Theodorsen, T.; Stickle, G.W. *Effect of a Trailing-Edge Extension on the Characteristics of a Propeller Section*; National Advisory Committee for Aeronautics: Washington, DC, USA, 1944.
2. Ito, A. The effect of trailing edge extensions on the performance of the Göttingen 797 and the Wortmann FX 63–137 aerofoil sections at Reynolds numbers between 3×10^5 and 1×10^6 . *Aeronaut. J.* **1989**, *93*, 283–289.
3. Yarusevych, S.; Sullivan, P.E.; Kawall, J.G. On vortex shedding from an airfoil in low-Reynolds-number flows. *J. Fluid Mech.* **2009**, *632*, 245–271. [[CrossRef](#)]
4. Huang, R.F.; Lin, C.L. Vortex shedding and shear-layer instability of wing at low-Reynolds numbers. *AIAA J.* **1995**, *33*, 1398–1403. [[CrossRef](#)]
5. Huang, R.F.; Lee, H.W. Turbulence effect on frequency characteristics of unsteady motions in wake of wing. *AIAA J.* **2000**, *38*, 87–94. [[CrossRef](#)]
6. Guan, Y.; Pröbsting, S.; Stephens, D.; Gupta, A.; Morris, S.C. On the wake flow of asymmetrically beveled trailing edges. *Exp. Fluids* **2016**, *57*, 78. [[CrossRef](#)]
7. Butler, S. Aircraft Drag Prediction for Project Appraisal and Performance Estimation. 1973. Available online: <http://discovery.nationalarchives.gov.uk/details/r/C10818307> (accessed on 2 August 2018).
8. Stanewsky, E. Adaptive wing and flow control technology. *Prog. Aerosp. Sci.* **2001**, *37*, 583–667. [[CrossRef](#)]
9. Neuhart, D.H.; Pendergraft, O.C., Jr. *A Water Tunnel Study of Gurney Flaps*; National Aeronautics and Space Administration (NASA): Washington, DC, USA, 1988.
10. Jang, C.S.; Ross, J.C.; Cummings, R.M. Numerical investigation of an airfoil with a Gurney flap. *Aircr. Des.* **1998**, *1*, 75. [[CrossRef](#)]
11. Storms, B.L.; Jang, C.S. Lift enhancement of an airfoil using a Gurney flap and vortex generators. *J. Aircr.* **1994**, *31*, 542–547. [[CrossRef](#)]
12. Traub, L.W. Examination of Gurney Flap Pressure and Shedding Characteristics. *J. Aircr.* **2017**, *54*, 1990–1995. [[CrossRef](#)]
13. Liu, T.; Montefort, J.; Liou, W.; Pantula, S.; Shams, Q. Lift enhancement by static extended trailing edge. *J. Aircr.* **2007**, *44*, 1939–1947. [[CrossRef](#)]
14. Lee, H.T.; Kroo, I.; Bieniawski, S. Flutter suppression for high aspect ratio flexible wings using microflaps. In Proceedings of the 43rd AIAA/ASME/ASCE/AHS/ASC Structures, Structural Dynamics, and Materials Conference, Denver, CO, USA, 22–25 April 2002; p. 1717.

15. Spedding, G.; McArthur, J. Span efficiencies of wings at low Reynolds numbers. *J. Aircr.* **2010**, *47*, 120–128. [[CrossRef](#)]
16. Rodríguez, I.; Lehmkuhl, O.; Borrell, R.; Oliva, A. Flow past a NACA0012 airfoil: from laminar separation bubbles to fully stalled regime. In *Direct and Large-Eddy Simulation IX*; Springer: Berlin, Germany, 2015; pp. 225–231.
17. McCormick, B.W. *Aerodynamics, Aeronautics, and Flight Mechanics*; Wiley: New York, NY, USA, 1995; Volume 2.
18. Ngo, H.T.; Barlow, L.E. Lifting Surface with Active Variable Tip Member and Method for Influencing Lifting Surface Behavior Therewith. U.S. Patent 6,394,397, 28 May 2002.
19. Anderson, J.D., Jr. *Fundamentals of Aerodynamics*; Tata McGraw-Hill Education: New York, NY, USA, 2010.
20. Bendat, J.S.; Piersol, A.G. *Random Data Analysis and Measurement Procedures*; Wiley: New York, NY, USA, 2000.
21. Mohsen, A.M. *Experimental Investigation of the Wall Pressure Fluctuations in Subsonic Separated Flows*; Technical Report; Boeing Commercial Airplane Co.: Renton, WA, USA, 1967.



© 2018 by the authors. Licensee MDPI, Basel, Switzerland. This article is an open access article distributed under the terms and conditions of the Creative Commons Attribution (CC BY) license (<http://creativecommons.org/licenses/by/4.0/>).